A&A 567, A68 (2014)
DOI: 10.1051/0004-6361/201423596

Astronomy & Astrophysics

Gas accretion from minor mergers in local spiral galaxies⋆

E. M. Di Teodoro[1] and F. Fraternali[1,2]

[1] Department of Physics and Astronomy, University of Bologna, 6/2, Viale Berti Pichat, 40127 Bologna, Italy
e-mail: enrico.diteodoro@unibo.it
[2] Kapteyn Astronomical Institute, Postbus 800, 9700 AV Groningen, The Netherlands

Received 7 February 2014 / Accepted 28 May 2014

ABSTRACT

We quantify the gas accretion rate from minor mergers onto star-forming galaxies in the local Universe using HI observations of 148 nearby spiral galaxies (WHISP sample). We developed a dedicated code that iteratively analyses HI data-cubes, finds dwarf gas-rich satellites around larger galaxies, and estimates an upper limit to the gas accretion rate. We found that 22% of the galaxies have at least one detected dwarf companion. We made the very stringent assumption that all satellites are going to merge in the shortest possible time, transferring all their gas to the main galaxies. This leads to an estimate of the maximum gas accretion rate of 0.28 $M_{\odot}\,\mathrm{yr}^{-1}$, about five times lower than the average star formation rate of the sample. Given the assumptions, our accretion rate is clearly an overestimate. Our result strongly suggests that minor mergers do not play a significant role in the total gas accretion budget in local galaxies.

Key words. galaxies: interactions – galaxies: evolution – galaxies: kinematics and dynamics – galaxies: star formation – galaxies: dwarf

1. Introduction

The evolution of galaxies is strongly affected by their capability of retaining their gas and accreting fresh material from the surrounding environment. Galaxies belonging to the so-called blue-sequence, which are actively forming stars and are dominated by young stellar populations, show an almost constant or a slowly declining star formation rate (SFR) throughout the Hubble time (e.g., Panter et al. 2007). Since the gas consumption time-scales are always of the order of a few Gyr (Noeske et al. 2007; Bigiel et al. 2011), spiral galaxies need to replenish their gas at rates similar to their star formation rates (Hopkins et al. 2008; Fraternali & Tomassetti 2012). These arguments are fully applicable to the Milky Way: with an SFR of 1−3 $M_{\odot}$ that slowly declined during the last ∼10 Gyr (e.g., Aumer & Binney 2009; Chomiuk & Povich 2011), the Galaxy would have exhausted its gas reservoir in a few Gyr without replacements from outside (e.g., Chiappini et al. 1997).

There are essentially two sources from which disc galaxies can gain new gas: the intergalactic medium (IGM) and other gas-rich galaxies. The IGM is the place where most baryons are thought to reside yet (e.g., Bregman 2007). Most of this gas is expected to be in a diffuse warm-hot phase (e.g., Shull et al. 2012). The IGM represents a huge reservoir of nearly pristine gas, but how this material can cool and accrete onto the discs is only poorly understood. Current cosmological simulations predict that gas accretion can occur in two modes (e.g., Ocvirk et al. 2008; Kereš et al. 2009): hot accretion, which dominates the growth of massive galaxies, and cold accretion through filamentary streams and clouds, which prevails in lower mass structures and at high redshifts (e.g., Dekel & Birnboim 2006).

The second channel for gas accretion is through merger events. According to the extended Press-Schechter theory, the structures in the Universe grow by several inflowing events and have increased their mass content through a small number of major mergers, more common at high redshifts, and through an almost continuous infall of dwarf galaxies (Bond et al. 1991; Lacey & Cole 1993). Although several theoretical (e.g., Stewart et al. 2009; Kazantzidis et al. 2009) and observational studies (e.g., Patton et al. 2000; Lotz et al. 2008; Lambas et al. 2012) have been carried out in the past years, predictions and estimates for the galaxy merger rate and its evolution with redshift remain uncertain and no consensus has been achieved yet (e.g., Bertone & Conselice 2009; Hopkins et al. 2010).

In this paper, we use neutral hydrogen (HI) observations to investigate gas accretion from minor mergers onto star-forming galaxies in the local Universe. The advantage of using HI observations instead of the optical-UV ones is that both morphological and kinematical information are immediately available. In addition, the gas layers are more easily disturbed by tidal interactions than the stellar disc. Two recent studies by Holwerda et al. (2011) and Sancisi et al. (2008) have taken advantage of HI data and used the WHISP catalogue (van der Hulst et al. 2001). Holwerda et al. (2011) focused on the galaxy merger fraction and, employing techniques developed for optical-UV observations, found a merger fraction of between 7% and 13%. Instead, Sancisi et al. (2008) attempted to quantify the contribution of minor mergers to the total gas accretion. They found that 25% of the local galaxies show signs of minor interactions or have disturbed HI distribution and, assuming lifetimes for these observed features of about 1 Gyr and a typical accreted HI mass of the order of 10^8–10^9 $M_{\odot}$, they calculated an accretion rate of about 0.1−0.2 $M_{\odot}\,\mathrm{yr}^{-1}$. This value is about an order of magnitude lower than typical star formation rates.

In this study, we use a quantitative approach to obtain a reliable estimate for the merger fraction and the gas accretion rate. We make use of a specific-purpose numerical code that is able to quickly analyse a large number of HI data-cubes, find dwarf

⋆ Appendix A is available in electronic form at http://www.aanda.org

gas-rich companions around disc galaxies, and estimate an upper limit for the gas accretion onto the discs. In Sect. 2, we describe the main features of our code and the methods we adopted. In Sect. 3, we show the results obtained by applying our analysis on a sub-sample of the WHISP catalogue, and we discuss them in Sect. 4.

2. Method

We wrote a numerical code to automatically identify 3D sources in data-cubes, that is, in image arrays with two spatial dimensions, related to the position on the plane of the sky, and one spectral dimension, which can correspond either to velocity or to frequency. Our code is targeted to work with HI observations as it performs a 3D scanning of the data to search for dwarf gas-rich companions around large galaxies. When the program has found a candidate, it derives its physical properties, such as the HI mass, the projected distance from the main galaxy, and an estimate of the accretion rate onto the central disc. In short, the code used in this work is essentially a source finder plus an algorithm for estimating the accretion rate.

The standard flow of our code can be outlined in three steps:

1. *Identifying the main galaxy*. The pixels that belong to the central galaxy emission are identified and isolated through an appropriate mask.
2. *Searching for dwarf galaxies*. The data-cube is scanned for 3D sources, and dwarf galaxies or HI clouds inside the field of view are identified.
3. *Estimating the gas accretion rate*. For each detected dwarf, a maximum accretion rate onto the disc is calculated by estimating a minimum time of collision between the satellite and the central galaxy.

In the following sections, we describe the most important steps and the main features and limitations of our code.

2.1. Searching for sources and background statistics

The searching algorithm is derived from *Duchamp*, a code dedicated to 3D source detection (Whiting 2012) that was developed for the Australian SKA Pathfinder (ASKAP). The basic idea behind this algorithm is to locate and connect groups of bright and contiguous pixels that lie above some flux threshold, without imposing any size or shape requirement on the detection. The search is performed using either a 2D raster-scanning algorithm (Lutz 1980) or a 1D research along each individual pixel spectrum. Three-dimensional sources (two spatial dimensions and one spectral) are then built up on the basis of adjacency or neighbourhood criteria both in the velocity and in the spatial domain. For a full description of the source-finding algorithm, we refer to the *Duchamp* main paper. The 1D technique is less computationally expensive, but it can bring spurious detections. In contrast, the Lutz algorithm is generally more reliable at the price of computational slowness. As discussed later in this section, we used the 1D method to identify the main galaxy emission and the 2D technique to detect companions.

The searching algorithm can be schematically summarized as follows:

1. *Pixel detection*. The data-cube is scanned using one of the above-mentioned techniques, and a list of all pixels with a flux higher than a given threshold is produced.
2. *Merging objects*. The detected pixels that are considered to lie close to each other based on spatial and spectral requirements are merged. Adjacent detections or detections lying within a user-defined range of pixels or channels are expected to belong to the same object. After this step, a list of 3D sources is produced.
3. *Growing objects*. The size of the detections is increased by adding pixels at the edges of the objects that are above some secondary threshold. This step guarantees a smooth transition between the source and the background.
4. *Rejecting objects*. Not all detected objects can be considered reliable. Sources that do not match some agreement criteria, such as a minimum number of contiguous pixels and channels, are discarded.

A crucial point of the searching algorithm is the determination of the flux threshold above which a pixel can be considered as a part of a source. To do this, the code needs to estimate the central value and width of the noise distribution in the data-cube. The former should be zero or very close to zero for HI data-cubes without systematics (due for instance to problems with the data reduction). The typical data-cube of the WHISP survey is dominated by a large number of noise pixels and a relatively small number of bright pixels that belong to the sources. In this situation, it is preferable to calculate the noise over the whole data-cube using the median as noise middle and the median absolute deviation from the median (MADFM) as noise spread. These quantities are less sensitive to the presence of very bright pixels than the equivalent normal statistics, the mean μ and the standard deviation σ. For a Gaussian distribution, the standard deviation can be written in terms of the MADFM as $\sigma = s/0.6745$ (for details, see Whiting 2012, and references therein). The threshold τ is then determined with a simple sigma-clipping, that is, it is set at a number n of standard deviations σ above the median m:

$$\tau = m + n\sigma. \quad (1)$$

This value is the minimum flux that a pixel must possess to be selected by the algorithm. We checked that the noise middle and spread calculated using the whole data-cube are the same as those obtained using only the channels with line emission; the differences do not exceed 5%.

We used the searching algorithms in two different steps: the identification of the main galaxy, and the detection of satellites. The former consists of isolating all regions that belong to the main galaxy emission. The code performs a search in the data-cube using the 1D technique and selects as the main galaxy the object that covers the largest number of pixels. This approach is not computationally expensive, and it is reliable when the code is analysing a heterogeneous group of galaxies, but it does not allow the code to identify systems in an advanced phase of merging, that is, when a companion is physically connected in space and velocity with the main galaxy. For the satellites, we used the Lutz algorithm, which guarantees a better reliability and minimizes the number of spurious detections. We imposed a neighbourhood criterion based on the spatial and spectral resolution of the observations: each detected pixel is merged with other detected pixels that lie within a spatial beam and within two velocity channels, which is the typical instrumental broadening full width at half maximum for HI observations when Hanning smoothing has been applied. Finally, we rejected all detections that are smaller than the beam area of the observations and less extended in velocity than the spectral broadening. We stress that a 3D source-finding algorithm, unlike the 2D methods, can isolate sources with different kinematics even if they are totally

or partially overlapped in the plane of the sky. Indeed, if two sources have radial velocities that differ by more than the typical velocity resolution ($\sim$10−15 km s^{-1}), they are always detected as separate sources, no matter whether or not they overlap in the sky.

2.2. Accretion and star formation rate estimates

The main purpose of this study is to estimate the maximum gas accretion rate attributable to minor mergers. In the following we describe our assumptions.

First, we assumed that all dwarf galaxies will collide in the future with the main galaxies and that their gas will be entirely and instantaneously accreted. Second, we assumed that the collision will occur in the shortest possible time. To calculate this time, we caused the satellites to move in parabolic trajectories leading to impact the outer regions of the main galaxies. The orbit was defined in the 3D space by fixing the focus of the parabola at the centre of the main galaxy, imposing the passage through the satellite and fixing the position of the orbital pericentre at a distance equal to the maximum radius of the central galaxy (Fig. 1). For a generic conic orbit, the time-scale of collision can be obtained by using the equation of the true anomaly ν of celestial mechanics:

$$\int_0^{\nu} \frac{\mathrm{d}\nu'}{(1 - e\cos\nu')^2} = \sqrt{\frac{\mu}{p^3}}\,(t - T_0), \tag{2}$$

where e is the eccentricity of the orbit, T_0 is the time of the peri-centre passage, p is the semi-latus rectum of the conic section, and $\mu = G(M_{\rm main} + M_{\rm sat}) \sim GM_{\rm main}$ is the total dynamical mass of the system galaxy plus satellite multiplied by the gravitational constant G. The dynamical mass of the central galaxy $M_{\rm main}(R_{\rm max}) = G^{-1}v_{\rm c}(R_{\rm max})^2 R_{\rm max}$ is calculated within the maximum radius $R_{\rm max}$ of the source, estimated by the searching algorithm. The circular velocity $v_{\rm c}$ is obtained from the velocity widths of the HI global profiles at the 20% of the peak flux corrected for the inclination taken from the HyperLEDA catalogue. By solving the integral (2) for parabolic orbits ($e = 1$), one obtains the following formula, which describes the variation of the true anomaly ν as a function of time:

$$\tan\frac{\nu}{2} + \frac{1}{3}\tan^3\frac{\nu}{2} = \sqrt{\frac{\mu}{p^3}}\,(t - T_0), \tag{3}$$

where the semi-latus rectum for parabolic orbit is $p = 2R$, where R is the distance between the focus and the vertex of the parabola (Fig. 1).

By using Eq. (3), we can estimate the time of the peri-centre passage T_0 by calculating ν through a de-projection of the projected anomaly $\nu_{\rm p}$ of the dwarf galaxy measured in the plane of the sky. The accretion rate of cold gas onto a certain galaxy is then obtained by dividing the HI mass of each dwarf by its time of peri-centre passage:

$$\dot{M}_{\rm HI} = \sum_{i=0}^{n} M_{{\rm HI},i}/T_{0,i}, \tag{4}$$

where the sum is taken over all the detected companion galaxies. The HI mass $M_{\rm HI}$ is calculated from the flux density using the following relation (Roberts 1975):

$$M_{\rm HI} = 2.356\times10^5\, D^2 \int S(v)\,\mathrm{d}v, \tag{5}$$

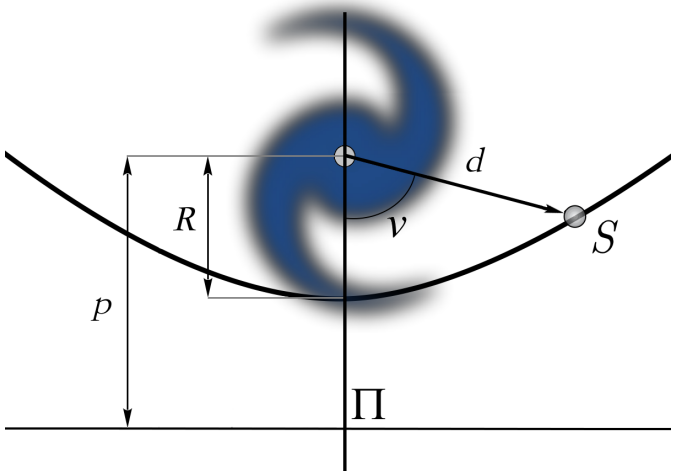

Fig. 1. Schematical view of the parabolic orbit approximation. The blue spiral is the main galaxy, S is the satellite with projected distance d and true anomaly ν. The distance p between the centre of the spiral galaxy and the directrix Π of the parabola is twice the outer radius of the main galaxy R.

where $\int S(v)\,\mathrm{d}v$ is the integral across the line of the flux density corrected for the primary beam attenuation and expressed in Jy km s^{-1} and D is the distance in Mpc. Equation (5) is valid under the assumption that the gas is optically thin, which is generally a good approximation for neutral hydrogen, especially in dwarf galaxies, therefore no correction for HI self-absorption was applied. The distances were preferably taken from the Extragalactic Distance Database (EDD, Tully et al. 2009), available for a number of galaxies with $v_{\rm sys}$ up to 10 000 km s^{-1} and mostly obtained from Cepheids, TRGB, SNIa, or the Cosmicflows-2 project (Tully et al. 2013). Otherwise, we used the NASA/IPAC Extragalactic Database (NED). For seven galaxies without available better estimates, we used the Hubble flow $D = v_{\rm sys}/H_0$ with $H_0 = 70$ km s^{-1} Mpc^{-1} and the systemic velocity $v_{\rm sys}$ corrected for Virgo-centric inflow using the values given by the HyperLEDA catalogue.

We compared the total gas accretion (4) with the gas depletion due to the star formation process in the discs. The SFR of the central galaxies was calculated from the far-infrared luminosities (Kennicutt 1998):

$$SFR = \frac{L_{\rm FIR}}{2.2\times10^{43}} \quad M_\odot\,{\rm yr}^{-1}, \tag{6}$$

with the $L_{\rm FIR}$ in erg s^{-1} obtained from the far-infrared (FIR) flux defined after Helou et al. (1985) as

$$\mathrm{FIR} = 1.26\times10^{-11}(2.58 f_{60\mu} + f_{100\mu}) \quad \mathrm{erg\,s^{-1}\,cm^{-2}}, \tag{7}$$

where $f_{60\mu}$ and $f_{100\mu}$ are the fluxes at 60 and 100 micron expressed in Jansky. In this work we used the IRAS fluxes taken from NED and HyperLEDA. All main galaxies in our sample are detected both at 60μ and 100μ. See Table A.1 for their main physical properties.

2.3. Major and minor mergers

We split major and minor mergers depending on the baryonic mass ratio: pairs of galaxies with $M_{\rm bar,sat}/M_{\rm bar,main} \leq 0.20$ are classified as minor mergers, otherwise as major. We preferably estimated the baryonic mass as

$$M_{\rm bar} = M_* + 1.4M_{\rm HI}, \tag{8}$$

where the factor 1.4 takes into account the helium gas fraction. We neglected the contribution of molecular gas. The HI mass $M_{\rm HI}$ is directly estimated from data-cubes through Eq. (5). A rough estimate of the stellar mass M_* is obtained by using the total $K_{\rm s}$-band magnitude, corrected for extinction, taken from the 2MASS Redshift Survey (2MRS, Huchra et al. 2012) and adopting the following formula (e.g. Longhetti & Saracco 2009):

$$\log_{10}(M_*) = \log_{10}(M/L_K) - 0.4[K + 5 - 5\log_{10}(D_{\rm [pc]}) - 3.28], \quad (9)$$

where M/L_K is the stellar mass-to-light ratio (in solar units) in the K band and 3.28 is the absolute K-band magnitude of the Sun in the Vega system (Binney & Merrifield 1998). We assumed a constant value of mass-to-light ratio $M/L_K = 0.6\,M_\odot/L_{\odot,K}$, compatible with stellar population models (e.g. Portinari et al. 2004) with a Kroupa initial mass function (Kroupa 2002).

When 2MRS magnitudes were not available, which is the case for most dwarf satellites and a few main galaxies, we directly derived $M_{\rm bar}$ from the baryonic Tully-Fisher relation (BTFR),

$$\log_{10}(M_{\rm bar}) = a\log_{10}(v_{\rm flat}) + b, \quad (10)$$

with $a = 3.82 \pm 0.22$ and $b = 2.01 \pm 0.41$ (McGaugh 2012). The $v_{\rm flat}$ was assumed as half of the inclination-corrected velocity widths w_{20} of the HI global profiles at the 20% of the peak flux. Since inclination angles are not known for most dwarf satellites, we adopted an average inclination of 60 degrees for these galaxies.

2.4. Data sample

The Westerbork HI survey of Irregular and Spiral galaxies Project (WHISP, van der Hulst et al. 2001) is a survey of the neutral hydrogen content in galaxies selected from the Uppsala General Catalogue (UGC, Nilson 1973) and is observed with the Westerbork Synthesis Radio Telescope (WSRT). To date, WHISP is the largest publicly available catalogue of HI nearby galaxies observed with an interferometer and includes galaxies at $\delta > 20°$ (B1950) with major axis apparent size $>1.2'$ (B band) and HI flux densities $F_{\rm HI} > 100$ mJy. Objects satisfying these selection criteria generally have systemic velocities lower than 6000 km s^{-1}, that is, distances smaller than 85 Mpc using the Hubble flow with $H_0 = 70$ km s^{-1} Mpc^{-1}. The galaxies were chosen to be reasonably distributed over all Hubble types, even if later-type galaxies are favoured by the observational criteria. The highest spatial resolution for the WHISP data is $12'' \times 12''/\sin(\delta)$, the typical channel separation is of the order of 5 km s^{-1}. In this work, we used HI data-cubes spatially smoothed to $30'' \times 30''$ and to $60'' \times 60''$. The original sample comprises 256 data-cubes containing about 370 galaxies[1].

Since our goal is to study dwarf satellites around large star-forming galaxies, we selected a sub-sample of spiral galaxies by keeping only the data-cubes that contained at least one galaxy with a rotation velocity $v_{\rm flat} = w_{20}/(2\sin i) > 100$ km s^{-1}. The selection was performed through a cross-correlation between the w_{20} estimated directly from the data-cubes and the w_{20} calculated using the Tully-Fisher relation from Sakai et al. (2000),

$$M_B = -(7.97 \pm 0.72)(\log w_{20} - 2.5) - (19.80 \pm 0.11), \quad (11)$$

[1] The datacubes, the column density maps, and the velocity fields of the WHISP galaxies, at 12″, 30″ and 60″ of resolution, are publicly available for the "Westerbork on the Web" project at ASTRON (http://www.astron.nl/wow/).

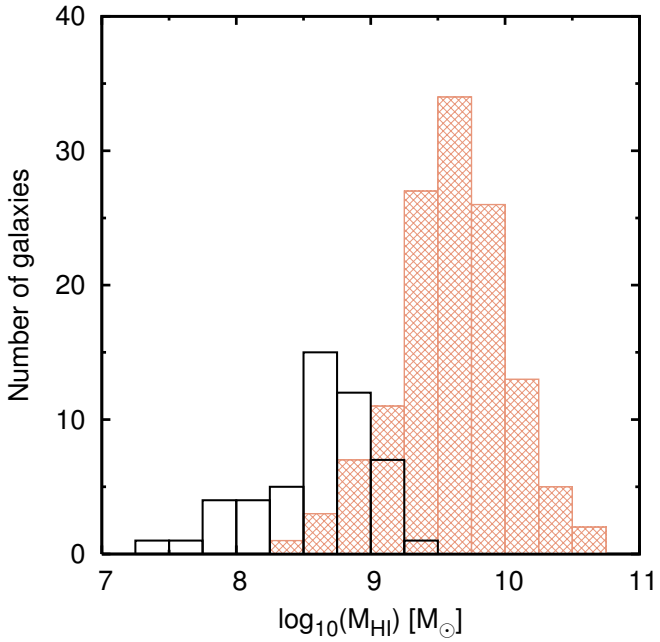

Fig. 2. HI mass distribution of the detected galaxies in the WHISP sample. Orange shadowed boxes show the spiral galaxies selected as $v_{\rm flat} > 100$ km s^{-1}, black boxes show their dwarf satellites.

where M_B is the B-band absolute magnitude (corrected for galactic extinction and k-correction), taken from HyperLEDA. We kept only galaxies for which both methods returned $v_{\rm flat} > 100$ km s^{-1}. This cross-correlation is needed to avoid spurious selections related to some unreliable inclination angles in the HyperLEDA catalogue. Our final sample has 148 data-cubes. Spiral galaxies therein have usually neutral hydrogen masses between 10^9 $M_\odot$ and few 10^{10} $M_\odot$ (Fig. 2). The global properties of the main galaxies are listed in Table A.1.

3. Results

We ran our code on data-cubes smoothed to 30″ and to 60″. The results obtained with these two data sets are thoroughly comparable. We fixed a sigma-clipping threshold for the source finder equal to 4 (see Eq. (1)) and a secondary threshold for growing objects at the edges of 2.5. After extensive experiments, these values appeared the best compromise between reaching low sensitivities and avoiding spurious detections.

We found that, among 148 data-cubes, 101 (~68.2%) had no detectable companions, whereas 47 (~31.8%) contained multiple systems. Among these 47 data-cubes, 15 (~10.1% of the total, ~31.9% of multiple systems) contained only galaxies with similar masses ($M_{\rm bar,sat}/M_{\rm bar,main} > 0.20$). Six data-cubes (~4.1% of the total, ~12.8% of multiple systems) show both major and minor companions, and 26 data-cubes (~17.6% of the total, ~55.3% of multiple systems) show only dwarf companions. Overall, among 148 analysed data-cubes, 21 (~14.2%), show companions that might be possible candidates for a future major merging, while 32 data-cubes (~21.6%) show potential candidates for minor mergers. Some examples of spiral galaxies with minor satellites are shown in Fig. 3.

We focused on potential minor mergers, and all data-cubes with only major companions were excluded from the further analysis. For the six data-cubes with both types of companions, we assumed as the main galaxy the one with the largest

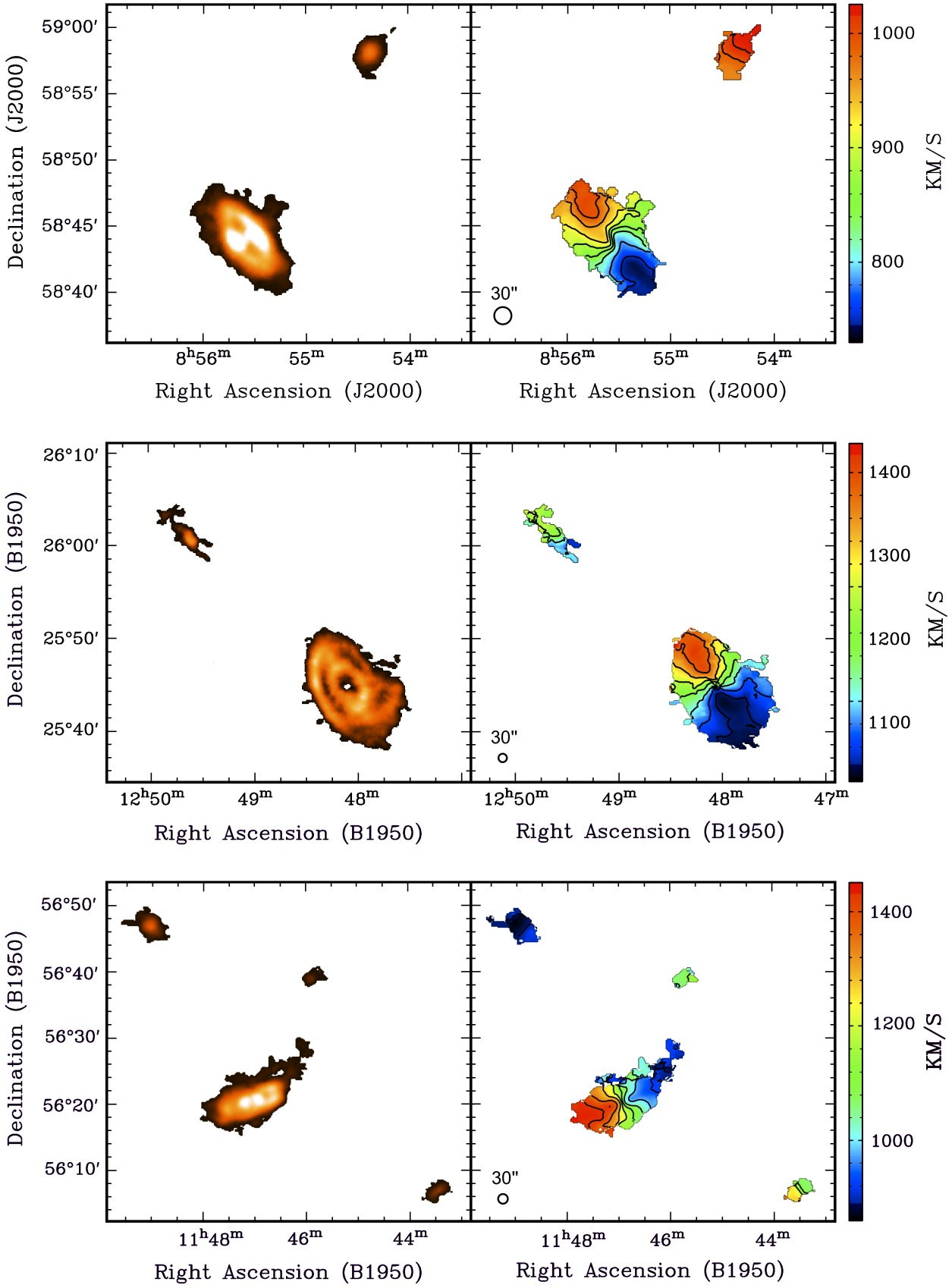

Fig. 3. Three examples of multiple systems in the WHISP sample. *From top* to *bottom*, UGC 4666, UGC 7989, UGC 6787 and their dwarf companions. In the *left panels*, the HI column-density maps (0th moment), in the *right panels*, the velocity fields (first moment) obtained from 30″ smoothed data-cubes.

Table 1. Detected companions of the WHISP spiral galaxies with $M_{\rm bar,sat}/M_{\rm bar,main} \leq 0.20$.

Name	Main galaxy	Coord. (J2000) RA–Dec	D	$v_{\rm sys}$	w_{20}	$M_{\rm HI}$	$d_{\rm proj}$	$t_{\rm coll}$	$\dot{M}_{\rm HI}$
			Mpc	km s^{-1}	km s^{-1}	$10^8\,M_\odot$	kpc	10^8 yr	$M_\odot$/yr
(1)	(2)	(3)	(4)	(5)	(6)	(7)	(8)	(9)	(10)
AGC 102802	UGC 485	J004702.7+301243	58.9	5296	85	9.08	117	15.7	0.58
AGC 113996	UGC 624	J010107.2+304052	78.3	4762	29	8.76	119	11.6	0.75
AGC 113884	UGC 624	J010000.3+302357	78.3	4717	96	5.04	391	17.8	0.28
[VH2008] J0101+4744	UGC 625	J010118.4+474432	28.3	2795	62	3.02	36	4.5	0.67
DF1†	UGC 1437	J015708.1+354825	54.5	4592	172	14.80	133	9.8	1.51
PGC 9994	UGC 2141	J030653.0+301542	24.7	812	43	7.37	75	5.6	1.32
PGC 2328690	UGC 2459	J030225.7+485452	32.4	2449	134	16.29	131	14.3	1.14
[KLT2208] HI J0302+352*	UGC 2487	J030210.5+351627	72.2	4967	55	15.43	351	18.1	0.85
[SOS2010] J0301491+3529012	UGC 2487	J030147.2+352839	72.2	4909	38	3.61	129	8.6	0.42
UGC 2813	UGC 2800	J034234.1+711828	16.1[1]	1381	62	0.99	33	4.2	0.24
HFLLZOA G136.96+14.21	UGC 2916	J040403.5+713707	68.0	4450	158	14.36	114	10.8	1.33
2MASX J04550438+3002212	UGC 3205	J045826.3+295653	47.6	3239	173	10.26	350	17.6	0.58
DF2†	UGC 3205	J045504.2+300209	47.6	3530	47	5.03	184	9.7	0.52
DF3†	UGC 3205	J045653.8+293602	47.6	3229	110	19.34	385	18.3	1.06
DF4†	UGC 3382	J055903.3+621719	67.2	4407	64	3.83	160	12.6	0.30
DF5†	UGC 3407	J060841.0+415647	39.3	3683	66	3.50	96	10.1	0.35
DF6†	UGC 3407	J060913.3+420104	39.3	3688	114	4.51	48	7.9	0.57
DF7†	UGC 3407	J060853.9+420338	39.3	3693	73	0.80	27	3.5	0.23
DF8†,*	UGC 3422	J061633.1+705743	77.2	4009	24	3.22	238	9.8	0.33
GALEXASC J061256.68+710650.6	UGC 3422	J061254.8+710659	77.2	3998	104	5.52	83	7.5	0.74
NPM1G +60.0018	UGC 3546	J065150.2+604122	17.9	1768	52	1.12	58	5.8	0.19
GALEXASC J070643.91+635521.0	UGC 3642	J070645.1+635515	67.3	4714	106	3.56	169	11.1	0.32
UGC 3660	UGC 3642	J070634.1+635056	67.3	4261	75	8.70	350	17.9	0.49
KUG 0829+227B	UGC 4458	J083247.7+223443	68.6	4621	231	12.80	105	12.4	1.03
MCG +10-13-030	UGC 4666	J085422.1+585908	16.0	1016	90	1.26	69	5.7	0.22
SDSS J091001.72+325659.8	UGC 4806	J091005.0+325607	25.5	2021	125	4.23	89	9.5	0.45
KUG 0906+333A	UGC 4806	J090919.5+330734	25.5	1856	60	1.88	18	5.7	0.33
SDSS J093137.13+292533.3	UGC 5060	J093138.0+292534	24.0	1608	77	0.53	117	9.9	0.05
KDG 059	UGC 5253	J095156.6+720439	16.6	1121	46	2.03	57	6.2	0.33
UGC 6797	UGC 6778	J114940.5+482533	17.1	962	81	7.28	87	8.5	0.86
SDSS J115027.42+490105.9	UGC 6778	J115027.4+490106	17.1	1120	31	1.67	138	11.2	0.12
UGC 6791	UGC 6786	J114923.6+264428	22.5[1]	1866	274	5.38	111	10.0	0.54
SDSS J114820.16+562045.7	UGC 6787	J114820.6+562049	22.1	1080	28	0.62	105	7.6	0.08
UGC 6733	UGC 6787	J114535.7+555313	19.1[2]	1158	187	5.26	130	10.3	0.51
UGC 6816	UGC 6787	J115047.5+562719	17.1[1]	887	115	5.78	146	11.0	0.52
SDSS J122442.59+544441.3	UGC 7506	J122440.2+544448	36.0	2495	109	2.18	154	11.6	0.19
UGC 8005	UGC 7989	J125149.1+254644	14.3[1]	1196	198	8.84	101	8.6	1.02
UGC 8254	UGC 8307	J131038.2+363807	19.1	1088	105	3.71	149	16.1	0.23
DF9†,*	UGC 8307	J131153.6+362758	19.1[1]	954	75	1.92	100	14.2	0.14
UGC 8271	UGC 8307	J131131.3+361655	18.5[1]	1145	150	6.99	156	22.1	0.32
DF10†,*	UGC 8307	J131134.3+362942	19.1	1191	32	0.58	109	15.5	0.04
KUG 1309+362	UGC 8307	J131146.7+355731	19.1	1123	26	0.30	245	24.9	0.01
UGC 8303	UGC 8307	J131317.6+361303	18.5[1]	948	92	9.77	139	20.3	0.48
UGC 8314	UGC 8307	J131401.0+361908	19.1	938	71	1.06	113	21.2	0.05
MCG +08-27-001	UGC 9366	J143359.2+492647	38.9	2122	127	6.18	88	6.2	1.00
KUG 1512+557	UGC 9797	J151400.2+553222	46.6	3550	154	9.66	94	9.4	1.03
SDSS J152617.51+404004.0	UGC 9858	J152617.9+404008	32.2	2687	51	11.80	66	7.7	1.53
MCG +08-34-005	UGC 11283	J183400.4+492233	30.0	2076	63	3.75	51	7.5	0.50
GALEXASC J215645.61+275419.5	UGC 11852	J215645.7+275418	82.4	5710	46	5.30	221	15.2	0.35
ZOAG G095.92-08.72	UGC 11951	J221145.4+453649	14.2	1145	78	7.52	74	8.3	0.91

Notes. (1) First name in NED archive or DF if not classified; (2) UGC name of the main galaxy; (3) celestial coordinates; (4) adopted distance (same as the main galaxy or taken from EDD catalogue, when specified); (5) systemic velocity; (6) line width of the global profile at the 20% level; (7) total HI mass; (8) projected distance from the main galaxy; (9) time of collision with the main galaxy in a parabolic orbit; and (10) gas accretion rate onto the main galaxy. $^{(\dagger)}$ Not catalogued in the NED, HyperLEDA, or SIMBAD archives. $^{(*)}$ Without a clear optical/UV counterpart in DSS, SDSS or GALEX images. DF8 is not covered by the SDSS survey. $^{(1)}$ Distance from EDD catalogue.

HI mass and ignored the other spiral galaxies. Fifty dwarf gas-rich satellites are detected in total (Table 1). Forty-six dwarf galaxies have a clear optical counterpart in the Sloan Digital Sky Survey (SDSS) or in the Digitized Sky Survey (DSS) images. Four detections, marked with an asterisk in Table 1, are not unambiguously identifiable and might be either very faint dwarf galaxies or HI clouds. Most satellites are already catalogued in galaxy archives. Ten galaxies, marked with a dagger in Table 1,

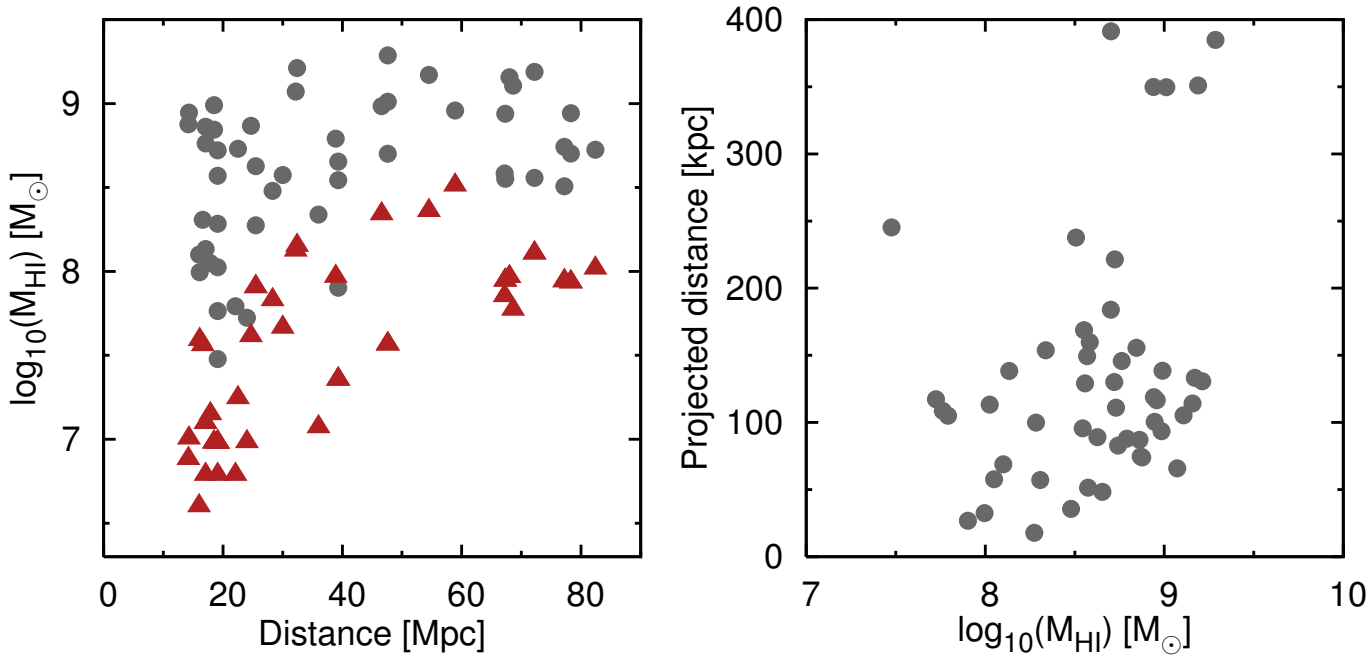

Fig. 4. *Left panel*, grey dots: HI masses of detected companions as a function of distance; red triangles: lowest detectable mass in the corresponding data-cubes. *Right panel*: distance from the main galaxies projected onto the plane of the sky of the detected satellites as a function of their HI mass.

do not seem to be catalogued. The HI masses of the detected dwarf galaxies vary between about $10^7\ M_\odot$ and few $10^9\ M_\odot$. The HI mass distribution of the main galaxies and their minor satellites is shown in Fig. 2. The mass function for spiral galaxies is peaked at $\log M_{\mathrm{HI}\,[M_\odot]} \sim 9.5$, consistently with studies on wider HI samples (e.g., Zwaan et al. 2005). Most dwarf companions have masses of a few $10^8\ M_\odot$ and their mass distribution has a cut-off above $5 \times 10^9\ M_\odot$. This is partially due to our selection criteria. However, it is interesting to note that this distribution is fairly similar to that of HI-rich dwarf galaxies in the Local Group and in Local Group analogues (e.g., Grcevich & Putman 2009; Pisano et al. 2011). In Fig. 4 we show the HI masses of the detected dwarf galaxies as a function of the distance from the Milky Way. The red triangles represent the minimum detectable mass for each data-cube, calculated using Eq. (5) on a 3D region with the size of a spatial beam times the velocity resolution (two channels) and a flux of 4× rms noise of the cube. This is the minimum mass that an object must have to be accepted by the source-finding algorithm. Note the bias effect on the detectable mass due to the distance (see discussion in Sect. 4.1).

The projected distances of the dwarf satellites from the main galaxies typically range from some dozens to a few hundred kiloparsecs, and typical time-scales for collisions, estimated through the parabolic orbit approximation, are between ∼100 Myr and 2 Gyr. The number of dwarfs within 100 kpc from the main galaxies and between 100 and 200 kpc is almost the same. In the right panel of Fig. 4 we show the projected distance as a function of the dwarf HI masses. Within 200 kpc, dwarf galaxies are quite uniformly distributed over the HI masses. There is a weak tendency for companions to be more massive at larger distances, as we may expect. However, there is an observational bias that can affect this plot. It is a combination of two effects: the linear field-of-view of the observations increases with distance, while the minimum detectable mass (Fig. 4, left panel) and the linear resolution decrease. Thus we may detect preferentially companions with lower masses closer to the main galaxies, and vice versa. Moreover, there is also a selection effect due to the primary beam attenuation, that is, at large angular distances, only massive systems are detected because of the lower sensitivity of the instrument. These effects make it difficult to compare our findings with studies of dwarfs galaxies in the Local Group.

The systemic velocity of dwarf galaxies is calculated as the average midpoint between the velocities at the 20% and 50% of the peak flux of their global HI profiles. The $\Delta v_{\mathrm{sys}} = \|v_{\mathrm{sys,main}} - v_{\mathrm{sys,sat}}\|$ ranges between a few tens to a few hundred $\mathrm{km\,s^{-1}}$. Satellites do not have systemic velocities that differ by more than 300 $\mathrm{km\,s^{-1}}$ from those of the main galaxies. The velocity widths w_{20} of dwarf galaxies, taken at the 20% of the peak flux, are usually lower than 200 $\mathrm{km\,s^{-1}}$, even if corrected for a mean inclination of 60 degrees, except for three galaxies. Overall, most of the satellites have $w_{20} < 100$ $\mathrm{km\,s^{-1}}$.

For each data-cube with identified dwarf companions, we calculated the maximum possible accretion rate of cold hydrogen gas $\dot{M}_{\mathrm{HI}}$ onto the main galaxy, the star formation rate $\dot{M}_{\mathrm{SF}}$ of the main galaxy, and the ratio $\dot{M}_{\mathrm{HI}}/\dot{M}_{\mathrm{SF}}$. For all galaxies, with or without identified companions, a potentially hidden accretion from dwarfs below the detectability limit was estimated. The hidden accretion rate was calculated by dividing the above-mentioned minimum detectable mass by the average collision time over the sample, that is, 1.1 Gyr. Integrating the HI mass function ($\phi_*[\mathrm{Mpc^{-3}\,dex^{-1}}\,h_{70}^3] = 4.8 \pm 0.3 \times 10^3$, $\log(M_*/M_\odot) + 2\log h_{70} = 9.96 \pm 0.02$ and $\alpha = -1.33 \pm 0.02$, Martin et al. 2010) below the detection limit and within the volume of each data-cube always gives HI masses lower than minimum detectable mass. Thus, with our choice we maximize the mass of the undetected galaxies.

We found a mean upper limit for the accretion in galaxies with identified minor companions of 0.86 $M_\odot\,\mathrm{yr^{-1}}$, with a mean ratio $\langle \dot{M}_{\mathrm{HI}}/\dot{M}_{\mathrm{SF}} \rangle \sim 0.67$. A more meaningful estimate is the mean upper limit to the accretion over the whole sample, however, which is $\dot{M}_{\mathrm{HI}} = 0.28\ M_\odot\,\mathrm{yr^{-1}}$ compared with the average star formation rate of 1.29 $M_\odot\,\mathrm{yr^{-1}}$, with a mean ratio $\langle \dot{M}_{\mathrm{HI}}/\dot{M}_{\mathrm{SF}} \rangle \sim 0.22$. The median of $\dot{M}_{\mathrm{HI}}/\dot{M}_{\mathrm{SF}}$ is 0.07. Thus,

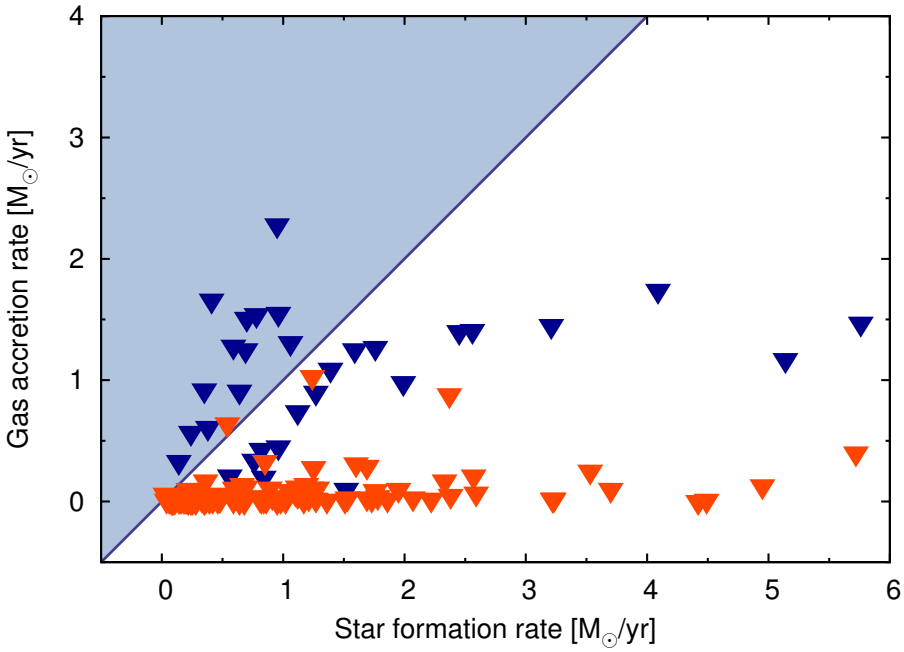

Fig. 5. Upper limits to the cold gas accretion rates from satellites vs star formation rates in spiral galaxies in the WHISP sample. The inverted dark blue triangles are upper limits to the gas accretion rate for galaxies with detected satellites (including both visible and hidden accretion), the inverted orange triangles are the hidden accretion upper limits for galaxies without companions, estimated as discussed in the text. The star formation rates are lower limits calculated from the far-infrared fluxes. The blue-shadowed region represents a complete feeding of SF through minor mergers.

the ratio of the gas needed for star formation to the maximum gas accretion provided by minor mergers is between 5 and 14. Considering a fraction of gas recycled from stellar feedback of 30% (e.g. Naab & Ostriker 2006) leads to a ratio between 3 and 10.

These results show that the number of dwarf galaxies in the local Universe is on average too low to guarantee the continuous gas replenishment needed by star formation. In Fig. 5 we show a plot of $\dot{M}_{\rm HI}$ versus $\dot{M}_{\rm SF}$ for each galaxy individually. If the gas accretion were high enough to sustain the star formation of the main galaxies, the data points would have fully populated the blue-shadowed region in the upper-left corner, whereas the vast majority lie well below the blue straight-line, indicating a ratio $\dot{M}_{\rm HI}/\dot{M}_{\rm SF} = 1$. We conclude that minor mergers cannot add enough gas to the discs and sustain star formation. Once again, our values of gas accretion rates are very strong upper limits because of our very stringent assumptions, and the real accretion rates might reasonably be one order of magnitude lower than our estimate. Incidentally, we note that our assumptions would imply that all dwarf galaxies disappear in the next 2 Gyr. We stress that our SFRs are very likely lower limits because they were calculated using only FIR fluxes. This bias goes in the direction of strengthening our findings.

We repeated the analysis of the WHISP data-cubes using a sigma-clipping threshold for the sources of 3σ and 5σ. Reducing the detection threshold leads the program to identify many more dwarf companions: more than 100 minor satellites are detected at the lower level, but most of these sources are clearly false detections and the results obtained are very likely unreliable. Such a large fraction of wrong detections is probably due to the low signal-to-noise of the WHISP data-cubes. Instead, increasing the detection threshold to 5σ leads to results very similar to those described above as just two of the dwarf companions found at 4σ are missed by the rejection criteria, namely the satellites of UGC 7506 and UGC 9858. These companions are actually good detections, as quoted in the literature (Noordermeer et al. 2005), but at a 5σ level they are discarded by the one-beam covering requirement. The mean values of the accretion rate at 5σ also agree with those found at 4σ.

4. Discussion

The application of our code to the WHISP catalogue led to a firm upper limit for the accretion of cold gas from minor mergers in the local Universe of 0.28 $M_\odot\,{\rm yr}^{-1}$. The total multiple system fraction for the WHISP sample is ~32%, in particular, ~22% of galaxies are accompanied by minor companions and ~14% are major systems. Here we discuss the main uncertainties of our results and their relevance.

4.1. Uncertainties

Our estimate does not take into account the molecular fraction. The amount of molecular gas in dwarf galaxies is highly unconstrained as they are often undetected in CO emission lines (e.g., Taylor et al. 1998). They also usually have low metallicities, making the conversion between CO and H_2 even more uncertain (e.g., Boselli et al. 2002). However, any realistic correction for molecular gas is not expected to increase our accretion rate by more than a factor two.

WHISP is a source-targeted survey, and it can obviously not be considered as a complete sample. The selection criterion, based on the apparent size of the observed galaxies, produces a catalogue that favours progressively larger and more massive galaxies moving to greater distances from the Milky Way. This effect can be appreciated in Fig. 4 (left panel), although it appears to be not too severe. The growth with the distance of the minimum detectable mass furthermore makes it impossible to detect low-mass satellites at large distances. To test the importance of these biases, we considered only data-cubes with a minimum detectable mass $M_{\rm det} \leq 10^8\ M_\odot$. In this way, we obtained a sub-sample of galaxies where satellites are quite uniformly distributed over the mass and the distance ranges (left panel of Fig. 4). The highest accretion rate obtained in this case is 0.21 $M_\odot\,{\rm yr}^{-1}$. Reducing the threshold to data-cubes with $\log M_{\rm det} \leq 5 \times 10^7\ M_\odot$ leads to a highest accretion rate of 0.18 $M_\odot\,{\rm yr}^{-1}$. These values indicate that our accretion rate estimates are not strongly affected by the incompleteness of the dwarf galaxy sample.

Another bias effect is related to the linear field of view, which is greater at larger distances. In the farthest systems, the field of view allows us to observe satellites with projected distances of some hundred kpc from the main galaxies, whereas we cannot go beyond one hundred kpc in the closest systems. The primary beam attenuation of the WSRT is significantly large (~80% of the flux is missed) beyond 25′ from the pointing centre, corresponding to ~70 kpc at about 10 Mpc. This indicates that we should be able to also detect fairly well-separated satellites in the nearest systems. The most distant satellites have longer collision time-scales, and their contribution to the global accretion is expected to be smaller. In our sample, considering only satellites within 100 kpc from the main galaxies gives an accretion rate of 0.38 $M_\odot\,\mathrm{yr}^{-1}$, 0.27 $M_\odot\,\mathrm{yr}^{-1}$ between 100 and 200 kpc and 0.21 $M_\odot\,\mathrm{yr}^{-1}$ beyond 200 kpc (the global value being 0.86 $M_\odot\,\mathrm{yr}^{-1}$) . These results show that the contribution of very distant satellites is progressively less important, thus the limited field of view of the closest systems probably does not significantly affect our accretion rate estimate.

In the literature, mergers are usually classified on the basis of their dynamical mass ratio: pairs of galaxies with $M_{\rm sat}/M_{\rm main} \leq 0.1-0.2$ are considered minor mergers, otherwise they are major mergers. Unfortunately, we cannot easily estimate the dynamical masses of satellite galaxies from the HI data. Thus, in this work, we divided satellites according to the ratio of their baryonic mass to the main galaxy baryonic mass. Satellites with baryonic content lower than 20% of the main galaxies ($M_{\rm bar,sat}/M_{\rm bar,main} \leq 0.20$) are classified as minor companions. This is an arbitrary but conservative choice, since most detected satellites have a mass ratio $\ll$0.05. It is interesting to quantify the accretion rate using different baryonic mass ratios, however. In our sample, the highest accretion rates range between 0.20 $M_\odot\,\mathrm{yr}^{-1}$ for $M_{\rm bar,s}/M_{\rm bar,g} \leq 0.1$ and 0.56 $M_\odot\,\mathrm{yr}^{-1}$ for $M_{\rm bar,sat}/M_{\rm bar,main} \leq 0.5$. If we consider all galaxy pairs as potential mergers and calculate the accretion rate by accreting the less massive ones onto the most massive ones, we obtain a value of 1.22 $M_\odot\,\mathrm{yr}^{-1}$. Even this excessive overestimate is of the same order as the mean SFR. We conclude that mergers in the local Universe cannot sustain the star formation in spiral galaxies.

4.2. Comparison with other estimates

The accretion of cold gas from minor mergers in the local Universe has been estimated by Sancisi et al. (2008), who visually inspected and compared total maps, velocity fields, and position-velocity diagrams for the WHISP galaxies. They found a minor-merger fraction of about 25%. Unlike our approach, they considered only systems that showed clear signs of tidal interactions, such as tails, bridges, disturbed HI morphologies, and/or kinematics. By assuming typical HI masses of the dwarfs of the order 10^{8-9} $M_\odot$ and a lifetime for observed features of about 1 Gyr, Sancisi et al. inferred a mean accretion rate of HI gas around 0.1–0.2 $M_\odot\,\mathrm{yr}^{-1}$ and stressed that this value is most likely a lower limit. It is worth noting that most systems we considered as potential minor mergers were not recognized by Sancisi et al. and, conversely, many interactions they identified were not found by our code. The reason is simple: our code searches for "separated" objects and treats all dwarf companions as candidates for minor mergers, including those that show no signs of ongoing interaction. In other words, we consider the population of dwarfs in the environment of a spiral galaxy that could become a minor merger in the near future. Our code identifies companions until the two galaxies start "touching" each other, and we estimate the accretion rate using the time-scale for collision as accretion time. Instead, Sancisi et al. (2008) found a later stage of merging, that is, when galaxies are strongly interacting and the gas is visibly disturbed in the morphology and/or in the kinematics. Consequently, they calculated the accretion rate using as time-scale the dynamical time that it should take for these features to disappear as the gas redistributes uniformly in the disc. In our work the accretion process ends when galaxies touch each other, whereas for Sancisi et al. (2008) that was the starting point. However, since the population of dwarf galaxies has most likely remained similar in the past Gyr or so, the two accretion rates should be similar. Interestingly, our upper limit of $\dot{M}_{\rm HI} < 0.28\ M_\odot\ \mathrm{yr}^{-1}$ does not contradict the average accretion rate estimated by Sancisi et al. (2008).

4.3. Merger fraction

Most studies recently published on the local merging systems have been made using images from optical-UV galaxy surveys (e.g., Patton et al. 2000; Lambas et al. 2012; Robotham et al. 2012) such as the Second Redshift Survey of Southern Sky (SRSS2), the Sloan Digital Sky Survey (SDSS) and the recent Galaxy And Mass Assembly (GAMA) survey, whereas just a few studies have been carried out using HI data (Sancisi et al. 2008; Holwerda et al. 2011). These studies have mainly investigated the fraction and the rate (fraction of mergers per comoving volume and time units) of galaxies showing signs of interactions and their evolution with time.

To date, two main approaches have been used to estimate the galaxy merger fraction, and both made use of high-resolution imaging. The pair method consists of counting the galaxies that are spatially separated from each other by less than a few tens of kpc and with spectroscopic radial velocities that do not differ by more than a few hundreds of $\mathrm{km\,s}^{-1}$ (e.g., Le Fèvre et al. 2000; Lin et al. 2008). Using this type of approach, it is possible to estimate a "progenitor galaxy" merger fraction. The second approach identifies mergers by quantifying morphological signatures that can be related to past or ongoing interactions, such as asymmetries and/or tails. This method makes use of several parameters to describe peculiar light distributions, such as the concentration-asymmetry-smoothness parameters (CAS, Conselice 2003) or the Gini-M_{20} parameters (Lotz et al. 2004). This technique can identify mergers in a relatively late stage, but not all asymmetric galaxies are necessarily merger features. The asymmetry method is similar to the technique used by Sancisi et al. (2008), whereas our approach on HI data-cubes is conceptually similar to the close-pairs method. The main difference is that we do not impose any limit for the projected distance between galaxies, whereas the velocity criterion is implicit in the data-cubes. Moreover, we select objects in 3D space (so potentially also overlapping in the sky) and we independently estimate the shortest collision time for each galaxy.

The asymmetry and close-pairs methods have been widely used with optical galaxy surveys, but, despite the large number of studies, there is little consensus on the galaxy merger rate and its evolution with redshift. Current observations of the fraction of galaxy undergoing a merger differ by an order of magnitude, from ~2% (e.g., Patton et al. 2000; De Propris et al. 2007, 2.3% and 1.9%, respectively) to 15% (e.g., de Ravel et al. 2009), and its trend with redshift varies from no evolution (e.g., Jogee et al. 2009) to strong evolution (e.g., López-Sanjuan et al. 2009). These discrepancies mainly arise from the different criteria for galaxy counting, merger selection, and bias in the galaxy samples. The value we found (~32%) is a companion fraction rather than a merger fraction as some companions that we considered

are fairly far away from the main galaxies (Fig. 4, right panel). It is therefore difficult to compare our fraction with the above-mentioned values. Broadly speaking, our estimate, which is indeed an upper limit, is higher at least by a factor 2–3 because our program treats all multiple systems as mergers and, working with HI data, more easily identifies dwarf gas-rich companions than is possible from optical observations. However, if we exclude the very far away companions, namely those beyond 100 kpc of projected distance, we obtain a companion fraction of ∼14%, not too different from the values found from optical studies. Finally, we stress that the WHISP sample is insignificant compared with other local references based on large catalogues, such as the SDSS or the Millennium Galaxy Catalogue (MGC), so that our values are less reliable from a statistical point of view.

A recent study carried out by Holwerda et al. (2011) estimated the merger fraction and rate for the whole WHISP sample using both the close-pairs and asymmetry methods on HI total maps. Holwerda et al. found a merger fraction of 7% based on pairs, and 13% based on disturbed morphology. We cannot compare our merger fraction with the latter value, because our program ignores the galaxy morphology, but the former value is fully comparable and our estimate is significantly higher by about a factor 4. A possible reason for this discrepancy is that Holwerda et al. based their pair fraction on 24 multiple systems previously identified and classified as interacting by Noordermeer et al. (2005b) and Swaters et al. (2002b), whereas our code detected many more satellites (see Table 1). If we use this sub-sample, the merger fractions become very similar.

4.4. Other channels for gas accretion

How star-forming galaxies can sustain their star formation is still an open question. In this study, we demonstrated that gas-rich minor mergers do not play a primary role and other dominant accretion channels must be considered. A way to fill the discrepancy between the estimated accretion rates and the SFRs could be to assume that the HI mass function were much steeper in the recent past than now, so that the number of dwarf satellites to be accreted were much higher. However, to date, no observational evidence in that direction can be achieved with the present generation of radio-telescopes, and the studies of the damped Lyman-α systems show a remarkable constancy of the HI mass throughout the Hubble time (e.g., Prochaska & Wolfe 2009). Another possibility is that most accretion is supported by infalling of gas clouds with HI masses of 10^7–$10^6\ M_\odot$, but recent deep observations of nearby groups of galaxies (e.g., Pisano et al. 2007; Chynoweth et al. 2009) as well as large blind surveys such as ALFALFA (Giovanelli et al. 2007) showed no evidence for a significant population of these small HI clouds. Moreover, studies of the Milky Way high-velocity clouds (HVCs) estimated a contribution to the total gas accretion of 0.1–0.2 $M_\odot\,\mathrm{yr}^{-1}$ (e.g., Wakker et al. 2007; Putman et al. 2012), a value much lower than the SFR. In addition, the gas in the ionized phase could produce an additional accretion rate of ∼1 $M_\odot\,\mathrm{yr}^{-1}$ (e.g., Shull et al. 2009), but it is not understood whether this gas can feed the star formation process in the disc. Numerical simulations (e.g., Fernàndez et al. 2012) support the idea that most of the gas infall in Milky Way-like galaxies is continuously provided by a drizzle and filamentary cosmological accretion, which would be almost undetectable or very difficult to identify (e.g., Lehner et al. 2013; Tumlinson et al. 2013). Finally, large amounts of matter could be supplied by the coronal gas cooling potentially triggered by supernova feedback (Marinacci et al. 2010).

5. Conclusions and future prospects

We estimated the maximum accretion of cold gas from minor mergers in a sample of large spiral galaxies from the WHISP catalogue. We used a source-finding algorithm to detect dwarf HI-rich satellites around these spiral galaxies and assumed that they will disappear and merge with the main galaxies in the shortest possible time. We found that ∼22% of galaxies have detected dwarf companions ($M_{\mathrm{bar,sat}}/M_{\mathrm{bar,main}} \leq 0.20$) and estimated a maximum gas accretion rate onto the main galaxies over the whole sample of 0.28 $M_\odot\,\mathrm{yr}^{-1}$. Given these assumptions, this value is a strong overestimate and the actual value can easily be an order of magnitude or more lower. From far-infrared luminosities, we calculated a mean star formation rate of 1.29 $M_\odot\,\mathrm{yr}^{-1}$, which is nearly five times higher than the maximum gas accretion rate. These results strongly suggest that minor mergers cannot bring enough gas to guarantee a long-lasting star formation process in the discs of the spiral galaxies. We note that our method can also detect, if present, large floating HI clouds and include them in the accretion budget. We did not find any significant population of these clouds. Thus, most of the gas accretion seems to be hidden from the current investigations in HI emission.

WHISP is a fairly large sample of nearby galaxies, but it is very small compared with surveys carried out at other wavelengths. The new generation of radio telescopes, such as the SKA (Carilli & Rawlings 2004) and its pathfinders, ASKAP (Johnston et al. 2008) and MeerKAT (Booth et al. 2009) and the restyling of existing interferometers, such as the WSRT with the APERTIF system (Verheijen et al. 2008) and the Karl G. Jansky VLA, will much increase the number of available data samples. In the next future, already scheduled HI surveys, such as WALLABY and DINGO with ASKAP, LADUMA with MeerKAT and WNSHS with WSRT/APERTIF, will increase the number of galaxies observed with radio interferometers by three orders of magnitude, from a few hundreds to about 10^5. It will be very interesting to apply the type of analysis performed in this paper to these large galaxy samples.

Acknowledgements. We thank Renzo Sancisi, Tom Oosterloo, Thijs van der Hulst and Micol Bolzanella for helpful suggestions and fruitful discussions. E.d.T. personally thanks Gabriele Pezzulli for his help. We used the WHISP data sample and the EDD, NED, HyperLEDA and Simbad catalogues. This research made use of some parts of the Duchamp code, produced at the Australia Telescope National Facility, CSIRO, by Matthew Whiting. We acknowledge financial support from PRIN MIUR 2010–2011, project "The Chemical and Dynamical Evolution of the Milky Way and Local Group Galaxies", prot. 2010LY5N2T.

References

Aumer, M., & Binney, J. J. 2009, MNRAS, 397, 1286
Bell, E. F., McIntosh, D. H., Katz, N., & Weinberg, M. D. 2003, ApJS, 149, 289
Bertone, S., & Conselice, C. J. 2009, MNRAS, 396, 2345
Bigiel, F., Leroy, A., Walter, F., et al. 2011, ApJ, 730, L13
Binney, J., & Merrifield, M. 1998, Galactic Astronomy (Princeton NJ: Princeton University Press)
Bond, J. R., Cole, S., Efstathiou, G., & Kaiser N. 1991, ApJ, 379, 440
Boselli, A., Lequeux, J., & Gavazzi, G. 2002, A&A, 384, 33
Booth, R. S., de Blok, W. J. G., Jonas, J. L., & Fanaroff, B. 2009 [arXiv:0910.2935]
Bregman, J. N. 2007, ARA&A, 45, 221
Naab, T., & Ostriker, J. P. 2006, MNRAS, 366, 899
Carilli, C. L., & Rawlings, S. 2004, New Astron. Rev., 48, 979
Chiappini, C., Matteucci, F., & Gratton, R. 1997, ApJ, 477, 765
Chomiuk, L., & Povich, M. S. 2011, AJ, 142, 197
Chynoweth, K. M., Langston, G. I., Holley-Bockelmann, K., & Lockman, F. J. 2009, AJ, 138, 287
Conselice, C. J. 2003, ApJS, 147, 1

Dekel, A., & Birnboim, Y. 2006, MNRAS, 368, 2
De Propris, R., Conselice, C. J., Liske, J., et al. 2007, ApJ, 666, 212
de Ravel, L., Le Fèvre, O., Tresse, L., et al. 2009, A&A, 498, 379
Fernàndez, X., Joung, M. R., & Putman, M. E. 2012, ApJ, 749, 181
Fraternali, F. 2010, AIPC, 1240, 135
Fraternali, F., & Binney, J. J. 2008, MNRAS, 386, 935
Fraternali, F., & Tomassetti, M. 2012, MNRAS, 426, 2166
Fraternali, F., van Moorsel, G., Sancisi, R., & Oosterloo, T. 2002, AJ, 123, 3124
Grcevich, J., & Putman, M. E. 2009, ApJ, 696, 385
Jogee, S., Miller, S. H., Penner, K., et al. 2009, ApJ, 697, 197
Johnston, S., Taylor, R., Bailes, M., et al. 2008, Exp. Astron., 22, 151
Kazantzidis, S., Zentner, A. R., Kravtsov, A. V., Bullock, J. S., & Debattista, V. P. 2009, ApJ, 700, 1896
Kennicutt, R. C. 1998, ApJ, 498, 541
Kereš, D., Katz, N., Fardal, M., Davé, R., & Weinberg, D. H. 2009, MNRAS, 395, 160
Giovanelli, R., Haynes, M. P., Kent, B. R., et al. 2007, AJ, 133, 2569
Heald, G., Józsa, G., Serra, P., et al. 2011, A&A, 526, A118
Helou, G., Soifer, B. T., & Rowan-Robinson, M. 1985, ApJ, 298, L7
Hess, K. M., Pisano, D. J., Wilcots, E. M., & Chengalur, J. N. 2009, ApJ, 699, 76
Holwerda, B. W., Pirzkal, N., de Blok, W. J. G., et al. 2011, MNRAS, 416, 2437
Hopkins, A. M., McClure-Griffiths, N. M., & Gaensler, B. M. 2008, ApJ, 628, L13
Hopkins, P. F., Croton, D., Bundy, K., et al. 2010, ApJ, 724, 915
Huchra, J. P., Macri, L. M., Masters, K. L., et al., 2012, ApJS, 199, 26
Kroupa, P. 2002, Science, 295, 82
Lacey, C., & Cole, S. 1993, MNRAS, 262, 627
Lambas, D. G., Alonso, S., Mesa, V., & O'Mill, A. L. 2012, A&A, 539, A45
Le Fèvre, O., Abraham, R., Lilly, S. J., et al. 2000, MNRAS, 311, 565
Lehner, N., Howk, J. C., Tripp, T. M., et al. 2013, ApJ, 770, 138
Leroy, A. K., Walter, F., Brinks, E., et al. 2008, ApJ, 136, 2782
Lin, L., Patton, D. R., Koo, D. C., et al. 2008, ApJ, 681, 232
Longhetti, M., & Saracco, P. 2009, MNRAS, 394, 774
López-Sanjuan, C., Balcells, M., & Pérez-González, P. G. 2009, A&A, 501, 505
Lotz, J. M., Primack, J., & Madau, P. 2004, AJ, 128, 163
Lotz, J. M., Davis, M., Faber, S. M., et al. 2008, ApJ, 672, 177
Lutz, R. K. 1980, The Comput. J., 23, 262
Martin, A. M., Papastergis, E., Giovanelli, R., et al. 2010, ApJ, 723, 1359
McGaugh, S. S. 2012, AJ, 143, 40
Nilson, P. 1973, Uppsala General Catalogue of Galaxies, Acta Universitatis Upsaliensis, Uppsala Astronomiska Observatoriums Annaler
Noeske, K. G., Faber, S. M., Weiner, B. J., et al. 2007, ApJ, 660, L47
Noordermeer, E., van der Hulst, J. M., Sancisi, R., Swaters, R. A., & van Albada, T. S. 2005, A&A, 442, 137
Marinacci, F., Binney, J. J., Fraternali, F., et al. 2010, MNRAS, 404, 1464
Okvirk, P., Pichon, C., & Teyssier, R. 2008, MNRAS, 390, 1326
Oosterloo, T., Fraternali, F., & Sancisi, R. 2007, AJ, 134, 1019
Panter, B., Jimenez, R., Heavens, A. F., & Charlot, S. 2007, MNRAS, 378, 1550
Patton, D. R., Carlberg, R. G., Marzke, R. O., et al. 2000, ApJ, 536, 153
Pisano, D. J., Barnes, D. G., Gibson, B. K., et al. 2007, ApJ, 662, 959
Pisano, D. J., Barnes, D. G., Staveley-Smith, L., et al. 2011, ApJS, 197, 28
Portinari, L., Sommer-Larsen, J., & Tantalo, R. 2004, MNRAS, 347, 691
Prochaska, J. X., & Wolfe, A. M. 2009, ApJ, 696, 1543
Putman, M. E., Peek, J. E. G., & Joung, M. R. 2012, ApJ, 749, 181
Rand, R. J., & Benjamin, R. A. 2008, ApJ, 676, 991
Roberts, M. S. 1975, in Galaxies and the Universe, ed. A. Sandage (University of Chicago Press), 309
Robotham, A. S. G., Baldry, I. K., Bland-Hawthorn, J., et al. 2012, MNRAS, 424, 1448
Sakai, S., Mould, J. R., Hughe, S. M. G., et al. 2000, ApJ, 529, 2, 698
Sancisi, R., Fraternali, F., Oosterloo, T., & van der Hulst, T. 2008, A&ARv, 15, 189
Shull, J. M., Jones, J. R., Danforth, C. W., & Collins, J. A. 2009, ApJ, 699, 754
Shull, J. M., Smith, B. D., & Danforth, C. W. 2012, ApJ, 759, 15
Stewart, K. R., Bullock, J. S., Wechsler, R. H., & Maller, A. H. 2009, ApJ, 702, 307
Taylor, C. L., Kobulnicky, H. A., & Skillman, E. D. 1998, AJ, 116, 2746
Tully, R. B., Rizzi, L., Shaya, E. J., et al., 2009, AJ, 138, 323
Tully, R. B., Courtois, H. M., Dolphin, A. E., et al. 2013, AJ, 146, 86
Tumlinson, J., Thom, C., Werk, J. K., et al. 2013, ApJ, 777, 59
van der Hulst, J. M., van Albada, T. S., & Sancisi, R. 2001, in Gas and Galaxy Evolution, eds. J. E. Hibbard, M. Rupen, & J. H. van Gorkom, ASP Conf. Ser. (San Francisco: ASP), 240, 451
Verheijen, M. A. W., Oosterloo, T. A., van Cappellen, W. A., et al. 2008, in The Evolution of Galaxies Through the Neutral Hydrogen Window, eds. R. Minchin, & E. Momjian, AIP Conf. Ser. (New York: Am. Inst. Phys.), 1035, 265
Wakker, B. P., York, D. G., Howk, J. C., et al. 2007, ApJ, 670, L113
Whiting, M. T. 2012, MNRAS, 421, 3242
Zwaan, M. A., Meyer, M. J., Staveley-Smith, L., & Webster, R. L. 2005, MNRAS, 359, L30

Pages 12 to 15 are available in the electronic edition of the journal at http://www.aanda.org

Appendix A: global properties of the main galaxies

In this Appendix, we list the main properties of the spiral galaxies selected from the WHISP sample for this work. Columns are as follows:

Column (1) gives the UGC name.

Column (2) provides an alternative common name, such as NGC, DDO, or IC classifications.

Column (3) provides the adopted distance in Mpc. We preferably used the EDD catalogue (Tully et al. 2009), otherwise, we used the following distance sources, in the given order: Cosmicflows-2 (Tully et al. 2013), NED archive, Hubble flow with $H_0 = 70$ km s^{-1} Mpc^{-1} and systemic velocities corrected for Virgo-infall taken from the HyperLEDA catalogue.

Columns (4) and (5) give the radius R_{25}, namely the length of the projected semi-major axis of a galaxy at the isophotal level 25 mag arcsec^{-2} in the B band. R_{25} is taken from the HyperLEDA catalogue. In Col. (4) the radius is listed in arcminutes, in Col. (5) it is converted into kiloparsecs using the distances in Col. (3).

Column (6) provides the inclination angle derived from the axis ratio in B band as listed in the HyperLEDA catalogue.

Column (7) gives the systemic velocity measured in this work as the average midpoint between the velocities at the 20% and 50% of the peak flux of the global HI-line profile.

Column (8) gives the HI-line width at the 20% of the peak flux of the global HI-line profile, as calculated in this work.

Column (9) provides the total HI mass estimated in this work.

Column (10) gives the adopted total baryonic mass $M_{\rm bar}$, calculated as described in Sect. 2.3.

Column (11) provides the star formation rate calculated from the 60 μm and 100 μm IRAS fluxes.

Column (12) gives the total gas accretion rate from minor mergers estimated in this work, including detectable and "hidden" accretion.

Table A.1. Global properties of the main galaxies selected from the WHISP sample.

UGC name	Other name	D	R_{25}	R_{25}	i	v_{sys}	w_{20}	M_{HI}	M_{bar}	SFR	$\dot{M}_{HI}$
		Mpc	$'$	kpc	$^\circ$	km s^{-1}	km s^{-1}	$10^9\,M_\odot$	$10^9\,M_\odot$	$M_\odot$/yr	$M_\odot$/yr
(1)	(2)	(3)	(4)	(5)	(6)	(7)	(8)	(9)	(10)	(11)	(12)
UGC 00094	NGC 0026	68.6[1]	0.56	11	47	4587	320	9.63	53.34	1.17	0.04
UGC 00232	–	65.3[2]	0.52	10	51	4837	275	7.61	38.40	1.95	0.10
UGC 00485	–	58.9[1]	1.15	20	83	5246	357	21.63	45.84	1.27	0.90
UGC 00528	NGC 0278	12.0	1.17	4	20	640	138	1.32	15.68	1.02	0.01
UGC 00624	NGC 0338	78.3[1]	0.87	20	68	4770	560	15.61	173.95	5.14	1.09
UGC 00625	IC 0065	28.3	1.29	11	73	2628	360	7.68	27.05	1.12	0.74
UGC 00690	–	74.5[1]	0.85	18	46	5872	325	9.61	56.80	0.54	0.64
UGC 00731	–	12.0	0.93	3	24	639	143	0.88	38.54[4]	0.21	0.01
UGC 00798	IC 1654	69.4[2]	0.50	10	40	4898	222	3.96	43.96	0.60	0.11
UGC 01013	NGC 0536	62.5[1]	1.48	27	69	5187	525	8.26	109.87	1.25	0.28
UGC 01256	NGC 0672	8.3	3.54	9	67	431	240	7.56	13.99	0.18	0.01
UGC 01437	NGC 0753	54.5[2]	0.69	11	51	4905	339	11.58	83.23	4.09	1.74
UGC 01550	NGC 0801	52.2[1]	1.38	21	78	5764	470	15.86	75.68	2.33	0.17
UGC 01633	NGC 0818	58.1[1]	1.09	18	70	4258	501	11.35	88.10	2.57	0.21
UGC 01810	–	109.8[3]	0.87	28	69	7578	602	31.64	210.16	2.37	0.88
UGC 01856	–	41.3[2]	1.07	13	81	4804	270	11.37	21.89	0.23	0.07
UGC 01886	–	67.4[2]	0.26	5	57	4854	502	25.67	121.29	0.85	0.33
UGC 01913	NGC 0925	9.2	5.36	14	58	552	222	3.85	12.90	0.64	<0.01
UGC 01993	–	107.7[1]	0.89	28	75	8018	526	13.70	95.49	1.24	1.03
UGC 02045	NGC 0972	21.7	1.66	10	61	1525	332	2.12	45.93	4.42	<0.01
UGC 02069	–	36.6[1]	0.62	7	55	3780	255	4.15	17.71	1.10	0.07
UGC 02080	IC 0239	10.0	2.13	6	24	902	135	5.46	11.52	0.16	0.01
UGC 02082	–	14.7	2.56	11	79	702	215	1.36	4.64	0.04	0.01
UGC 02141	NGC 1012	24.7	1.04	8	60	987	233	2.20	17.53	1.36	1.33
UGC 02154	NGC 1023	10.2	3.71	11	70	695	482	2.21	44.83	0.78	0.01
UGC 02183	NGC 1056	21.7	0.93	6	61	1540	290	3.65	18.80	0.98	0.01
UGC 02459	–	32.4	1.17	11	83	2467	337	12.30	31.48	0.59	1.28
UGC 02487	NGC 1167	72.2[3]	0.91	19	41	4953	468	16.65	261.23	3.21	1.36
UGC 02503	NGC 1169	32.4	1.66	16	54	2391	461	9.69	95.99	1.12	0.12
UGC 02800	–	18.9[1]	1.17	6	60	1187	217	2.01	5.05	1.52	0.25
UGC 02855	–	14.4[1]	1.77	7	65	1196	453	6.35	49.22	2.22	0.02
UGC 02916	–	68.0[2]	0.66	13	24	4517	336	23.12	94.12	2.45	1.40
UGC 03013	NGC 1530	25.4	0.91	7	55	2459	341	8.98	53.03	2.07	0.03
UGC 03137	–	22.1	1.90	12	78	993	216	4.41	9.32	0.15	0.02
UGC 03205	–	47.6[2]	0.66	9	66	3588	436	9.21	65.30	0.95	2.18
UGC 03326	–	77.6[1]	1.66	37	84	4060	532	19.48	135.84	2.38	0.05
UGC 03334	NGC1961	59.5[3]	2.23	39	50	3935	660	39.72	422.71	9.24	0.26
UGC 03354	–	52.5[1]	0.83	13	70	3085	441	8.89	68.85	3.22	0.02
UGC 03382	–	67.2[3]	0.63	12	21	4501	205	5.74	73.75	0.76	0.34
UGC 03407	–	39.3[2]	0.56	6	45	3602	312	1.75	22.06	0.70	1.17
UGC 03422	–	77.2[2]	0.91	20	62	4065	416	11.05	73.40	1.08	1.00
UGC 03546	NGC 2273	17.9	1.15	6	53	1836	339	1.95	19.09	0.56	0.21
UGC 03574	–	17.1	0.74	4	30	1441	150	3.21	6.70	0.35	0.02
UGC 03580	–	25.9	1.07	8	57	1198	236	3.81	12.87	0.48	0.02
UGC 03642	–	67.4[2]	0.76	15	41	4498	410	37.21	146.52	1.99	0.89
UGC 03734	NGC 2344	23.0	1.02	7	24	972	150	1.12	14.80	0.11	0.01
UGC 03759	NGC 2347	88.3[1]	0.83	21	44	4416	468	22.39	200.89	5.72	0.40
UGC 03993	–	66.3[3]	0.42	8	24	4365	175	7.13	50.87	0.91	0.04
UGC 04036	NGC 2441	44.7[1]	1.00	13	24	3469	141	4.07	31.61	0.89	0.11
UGC 04165	NGC 2500	15.0	1.23	5	25	515	113	0.97	6.82	0.35	<0.01
UGC 04256	NGC 2532	51.6[2]	0.83	12	34	5256	175	6.73	56.96	3.70	0.10
UGC 04273	NGC 2543	26.3	1.23	9	62	2473	317	4.32	20.75	1.23	0.11
UGC 04284	NGC 2541	11.2	1.51	5	59	559	210	4.91	8.32	0.08	<0.01
UGC 04458	NGC 2599	68.6[3]	0.77	15	32	4757	285	12.52	128.09	1.39	1.09
UGC 04605	NGC 2654	22.7	2.23	15	78	1354	430	6.32	35.50	0.82	0.01
UGC 04666	NGC 2685	16.0	2.18	10	58	876	303	1.96	17.39	0.14	0.22
UGC 04806	NGC 2770	25.5	1.73	13	76	1945	353	5.42	19.53	0.64	0.85
UGC 04838	NGC 2776	36.0	1.07	11	65	2626	202	6.24	44.41	1.53	0.03
UGC 04862	NGC 2782	42.1	1.62	20	42	2540	196	4.12	67.81	4.49	0.01

Notes. [(1)] Distance from Cosmicflows-2 catalogue. [(2)] Distance from NED catalogue. [(3)] Distance from Hubble flow with Virgo-infall corrected systemic velocity. [(4)] Baryonic mass from the baryonic Tully-Fisher relation.

Table A.1. continued.

UGC name	Other name	D	R_{25}	R_{25}	i	v_{sys}	w_{20}	M_{HI}	M_{bar}	SFR	$\dot{M}_{HI}$
		Mpc	$'$	kpc	$^\circ$	km s^{-1}	km s^{-1}	$10^9\,M_\odot$	$10^9\,M_\odot$	$M_\odot$/yr	$M_\odot$/yr
(1)	(2)	(3)	(4)	(5)	(6)	(7)	(8)	(9)	(10)	(11)	(12)
UGC 05060	NGC 2893	24.0	0.51	4	36	1700	187	0.92	6.66	0.42	0.05
UGC 05079	NGC 2903	8.5	6.01	15	63	555	390	3.95	39.88	0.95	<0.01
UGC 05251	NGC 3003	19.6[1]	2.39	14	77	1481	294	8.89	20.10	0.40	0.02
UGC 05253	NGC 2985	16.6	1.82	9	36	1324	316	11.62	55.21	0.82	0.37
UGC 05351	NGC 3067	20.6	1.02	6	71	1487	281	0.91	15.67	1.17	0.01
UGC 05452	NGC 3118	20.6	1.04	6	78	1348	216	3.41	5.91	0.07	0.02
UGC 05459	–	25.8	1.90	14	79	1108	282	4.82	18.06	0.48	0.02
UGC 05532	NGC 3147	39.8	2.04	24	29	2812	390	9.50	227.06	4.95	0.13
UGC 05556	NGC 3187	26.4	1.12	9	71	1582	276	1.09	5.48	0.48	0.06
UGC 05557	NGC 3184	13.0	3.71	14	21	593	146	3.95	32.47	0.20	0.01
UGC 05589	NGC 3206	25.8	1.15	9	59	1162	182	2.61	6.50	0.03	0.06
UGC 05685	NGC 3254	21.8	1.17	7	72	1359	378	4.71	24.34	0.22	0.10
UGC 05717	NGC 3259	24.0	0.85	6	58	1675	242	6.34	14.71	0.43	0.05
UGC 05786	NGC 3310	20.0	0.95	6	40	989	221	3.36	17.42	3.23	0.02
UGC 05789	NGC 3319	13.3	1.82	7	61	739	215	3.36	6.76	0.06	0.01
UGC 05840	NGC 3344	10.0	3.38	10	25	589	175	3.01	17.40	0.25	<0.01
UGC 05906	NGC 3380	26.1	0.77	6	27	1600	130	0.42	9.70	0.15	0.01
UGC 05909	NGC 3381	25.7	1.00	7	26	1633	146	2.12	9.07	0.34	0.02
UGC 05918	–	10.0	1.23	4	12	338	78	0.25	0.57	0.09	<0.01
UGC 05997	NGC 3403	20.2	1.38	8	68	1261	303	4.09	12.89	0.46	0.03
UGC 06024	NGC 3448	24.0	1.48	10	73	1369	299	6.76	21.06	1.12	0.05
UGC 06128	NGC 3512	26.1	0.79	6	29	1388	187	0.98	13.03	0.35	0.01
UGC 06225	NGC 3556	9.6	1.99	6	65	698	341	3.48	22.10	0.81	0.02
UGC 06263	NGC 3583	33.0	1.12	11	56	2134	346	6.65	69.34	2.59	0.07
UGC 06283	NGC 3600	14.4	0.93	4	72	713	218	2.86	6.14	0.26	0.01
UGC 06537	NGC 3726	17.1	2.62	13	47	864	284	5.05	35.11	0.46	0.01
UGC 06621	NGC 3786	40.0	0.97	11	59	2745	418	4.56	42.88	1.27	0.02
UGC 06778	NGC 3893	17.1	1.35	7	58	968	311	4.76	31.95	1.59	0.99
UGC 06786	NGC 3900	22.5	1.29	8	61	1801	426	3.33	25.43	0.24	0.56
UGC 06787	NGC 3898	22.1	1.73	11	54	1170	446	3.96	57.99	0.96	1.12
UGC 06833	NGC 3930	12.6	1.35	5	42	918	161	0.99	7.00	0.36	0.01
UGC 06870	NGC 3953	19.2[1]	3.09	17	62	1051	403	2.35	72.36	0.30	0.09
UGC 06884	NGC 3963	49.1[2]	1.26	18	27	3189	131	8.21	68.56	1.76	0.09
UGC 06930	–	17.1	0.71	4	42	778	141	2.52	4.77	0.19	0.01
UGC 06964	NGC 4010	19.1[1]	1.55	9	78	905	278	1.40	8.52	0.28	0.01
UGC 07030	NGC 4051	17.2	2.45	12	40	704	241	1.43	33.28	0.86	0.01
UGC 07081	NGC 4088	14.5[1]	3.54	15	68	756	381	4.15	32.18	1.51	0.01
UGC 07095	NGC 4100	20.3[1]	2.29	14	74	1075	402	3.02	35.53	1.21	0.03
UGC 07183	NGC 4157	18.0	3.08	16	80	771	422	6.29	54.12	1.69	0.03
UGC 07222	NGC 4183	16.4[1]	2.13	10	81	931	247	2.95	7.98	0.20	0.01
UGC 07256	NGC 4203	15.1	1.69	7	65	1088	270	2.34	33.99	0.10	<0.01
UGC 07321	–	6.0	2.39	4	86	407	210	0.34	0.72	0.08	0.01
UGC 07399	NGC 4288	9.2	0.85	2	41	535	165	0.74	1.35	0.35	0.01
UGC 07483	NGC 4359	16.3	0.69	3	53	1271	199	1.13	3.14	0.21	0.01
UGC 07489	NGC 4369	11.2	1.00	3	17	1029	88	0.43	4.83	0.33	0.02
UGC 07506	NGC 4384	36.0	0.63	7	39	2532	176	1.13	12.87	0.84	0.20
UGC 07766	NGC 4559	8.7	5.24	13	63	814	256	5.43	16.21	0.22	<0.01
UGC 07989	NGC 4725	12.4	4.89	18	45	1210	398	5.02	71.56	1.06	1.03
UGC 08307	NGC5033	19.1[1]	9.77	54	65	875	425	10.43	88.98	1.76	1.27
UGC 08403	NGC 5112	18.5	1.51	8	52	969	215	3.12	8.53	0.35	0.01
UGC 08699	NGC 5289	30.9	1.17	11	72	2518	352	2.76	18.81	0.23	0.02
UGC 08709	NGC 5297	30.9	1.86	17	76	2405	414	12.73	50.61	1.05	0.09
UGC 08711	NGC 5301	20.2	1.99	12	78	1508	336	3.56	18.33	0.81	0.04
UGC 08863	NGC 5377	28.0	1.82	15	67	1791	382	2.24	47.16	0.42	0.01
UGC 08900	NGC 5395	52.7[2]	1.26	19	62	3458	565	11.21	143.67	3.53	0.25
UGC 09242	–	27.9	2.08	17	86	1438	215	3.20	6.43	0.21	0.01
UGC 09366	NGC 5676	38.9	1.82	21	63	2121	462	6.41	137.46	5.76	1.09
UGC 09431	NGC 5714	38.7[1]	1.41	16	80	2242	356	7.51	29.58	0.66	0.14
UGC 09644	–	97.9[3]	0.57	16	20	6664	136	7.12	42.84	1.28	0.11
UGC 09753	NGC 5879	15.5	1.90	9	68	771	287	1.32	10.88	0.28	0.01
UGC 09797	NGC 5905	46.6[1]	1.62	22	50	3393	374	22.70	73.72	2.56	1.25
UGC 09858	–	32.2	1.95	18	78	2615	386	10.67	28.75	0.41	1.66
UGC 09969	NGC 5985	43.7	1.99	25	60	2515	542	10.76	144.58	1.19	0.14

Table A.1. continued.

UGC name	Other name	D	R_{25}	R_{25}	i	v_{sys}	w_{20}	M_{HI}	M_{bar}	SFR	$\dot{M}_{HI}$
		Mpc	$'$	kpc	$^\circ$	km s^{-1}	km s^{-1}	$10^9\,M_\odot$	$10^9\,M_\odot$	$M_\odot$/yr	$M_\odot$/yr
(1)	(2)	(3)	(4)	(5)	(6)	(7)	(8)	(9)	(10)	(11)	(12)
UGC 10359	NGC 6140	16.0	1.04	5	44	908	221	5.41	11.61	0.14	0.01
UGC 10445	–	18.1	0.95	5	45	962	159	2.23	6.94	0.16	0.05
UGC 10448	NGC 6186	154.0[2]	0.79	35	41	11352	118	9.56	439.96	8.82	0.02
UGC 10470	NGC 6217	23.0	1.12	7	34	1355	192	5.94	30.66	1.86	0.02
UGC 10497	–	65.6[2]	0.59	11	65	4296	267	8.93	21.34	0.36	0.17
UGC 10564	NGC 6237	21.0	0.62	4	52	1129	175	5.64	11.08	0.27	0.03
UGC 11124	–	25.0	1.12	8	26	1599	153	2.23	11.71	0.16	0.03
UGC 11218	NGC 6643	20.6	1.66	10	61	1484	350	3.20	30.27	1.78	0.04
UGC 11269	NGC 6667	44.9	0.93	12	56	2581	412	13.36	66.90	1.73	0.02
UGC 11283	IC 1291	30.0	0.66	6	35	1946	198	2.55	9.44	0.38	0.55
UGC 11429	NGC 6792	62.2[1]	1.04	19	58	4637	510	12.26	129.81	1.60	0.31
UGC 11466	–	18.1	0.74	4	53	821	237	2.79	10.96	0.84	0.01
UGC 11670	NGC 7013	15.0	2.08	9	71	775	340	1.35	26.16	0.28	<0.01
UGC 11852	–	82.4[2]	0.46	11	44	5845	328	26.73	82.67	0.96	0.45
UGC 11861	–	14.4	0.89	4	61	1482	259	2.10	10.25	0.47	0.02
UGC 11909	–	14.1	1.00	4	78	1105	242	2.87	7.78	0.39	0.01
UGC 11914	NGC 7217	15.0	2.29	10	35	950	301	0.70	52.88	0.68	<0.01
UGC 11951	NGC 7231	14.2	0.85	4	69	1086	223	1.56	4.97	0.35	0.92
UGC 11994	–	65.8[1]	1.04	20	82	4882	436	6.95	57.44	1.69	0.29
UGC 12554	NGC 7640	9.9	4.06	12	78	363	238	3.05	8.78	0.24	<0.01
UGC 12693	–	60.5[1]	0.55	10	78	4958	236	9.67	15.50	0.69	0.12
UGC 12732	–	15.1	1.38	6	28	728	131	1.96	4.06	0.59	0.01
UGC 12754	NGC 7741	13.6[1]	1.82	7	49	749	202	1.78	5.76	0.36	0.01
UGC 12808	NGC 7769	61.5[3]	0.87	16	68	4225	326	4.79	134.32	6.21	0.05